



Bridging Au nanoclusters with ultrathin LDH nanosheets via ligands for enhanced charge transfer in photocatalytic CO₂ reduction

Yanan Bo^{a,b,1}, Pengye Du^{a,1}, Hao Li^{c,1}, Rong Liu^c, Chengming Wang^a, Hengjie Liu^a, Dong Liu^{a,d,*}, Tingting Kong^{c,**}, Zhou Lu^{c,**}, Chao Gao^{a,**}, Yujie Xiong^{a,b,c,*}

^a Hefei National Research Center for Physical Sciences at the Microscale, Collaborative Innovative Center of Chemistry for Energy Materials (iChEM), School of Chemistry and Materials Science, University of Science and Technology of China, Hefei, Anhui 230026, China

^b Institute of Energy, Hefei Comprehensive National Science Center, 350 Shushanhu Rd., Hefei, Anhui 230031, China

^c Anhui Engineering Research Center of Carbon Neutrality, Anhui Province Key Laboratory of Optoelectronic Material Science and Technology, College of Chemistry and Materials Science, School of Physics and Electronic Information, Key Laboratory of Functional Molecular Solids, Ministry of Education, Anhui Normal University, Wuhu, Anhui 241002, China

^d Suzhou Institute for Advanced Research, University of Science and Technology of China, Suzhou, Jiangsu 215123, China

ARTICLE INFO

Keywords:

Au nanocluster
Layered double hydroxide
Bridging ligand
Charge transfer dynamics
Photocatalytic CO₂ reduction

ABSTRACT

Au nanoclusters (NCs) bring new opportunities for constructing visible-light photocatalysts for solar-driven CO₂ conversion, whereas the agglomeration under illumination and lack of catalytic sites severely hinder their application. One promising approach to address the limitations is the confinement of Au NCs on a heterogeneous substrate with efficient catalytic sites, in which a concomitant bottleneck originates from the electron transfer between Au NCs and catalytic sites determining the charge transfer dynamics. Herein, we develop an effective strategy for grafting Au NCs onto ultrathin layered double hydroxide (LDH) nanosheets via engineering bridging ligands. The bridging ligands function as both surface anchors and electron mediators, which confine and stabilize Au NCs on LDH, as well as facilitate electron transfer from Au NCs to catalytic sites. As a result, the durability and efficiency for photocatalytic CO₂ reduction is significantly enhanced. This work provides a fresh hint for stabilizing ultrasmall nanoclusters and facilitating the electron transfer between light-harvesting nanoclusters and catalytic sites through bridging ligands.

1. Introduction

Solar-driven CO₂ reduction into valuable chemical fuels such as CH₄, CO and CH₃OH is a promising approach to fulfilling carbon neutrality [1–5]. Developing efficient photocatalysts with superior light-harvesting ability and abundant active sites is crucial for CO₂ photoreduction [6,7]. When serving as light absorbers, pristine semiconductors or photosensitizers often exhibit low catalytic activity due to the lack of catalytic sites [8–11]. However, the introduction of catalytic sites by modifying semiconductors commonly affects the electronic structures, charge separation and transfer, which in turn leads to the variation of photocatalytic activity and selectivity [12,13]. This intricate

relationship necessitates the exploration of alternative light absorbers.

Metal nanoclusters, a form of ultrasmall metal assembly made up of a metal core and peripheral ligand, have recently gained popularity due to their unique physiochemical characteristics [14–16]. Their quantum size effect results in discrete energy levels, which makes them perform uniquely compared to their nanoparticle counterpart with continuous electronic bands [17]. As such, metal nanoclusters behave similarly to molecular complexes whose light absorption can be readily modulated and thus have great potential as visible-light absorbers in photocatalytic and photovoltaic systems [18,19]. Recently, thiolate-protected metal clusters, represented by glutathione-capped Au NCs (Au-GSH), have emerged as photosensitizers for extended light absorption, and the

* Corresponding authors at: Hefei National Research Center for Physical Sciences at the Microscale, Collaborative Innovative Center of Chemistry for Energy Materials (iChEM), School of Chemistry and Materials Science, University of Science and Technology of China, Hefei, Anhui 230026, China.

** Corresponding authors.

E-mail addresses: dongliu@ustc.edu.cn (D. Liu), 2022045@ahnu.edu.cn (T. Kong), zhoulu@ahnu.edu.cn (Z. Lu), gaoc@ustc.edu.cn (C. Gao), yjxiong@ustc.edu.cn (Y. Xiong).

¹ These authors equally contributed to this work.

photoexcited electrons from Au-GSH can trigger water splitting [18,20,21]. Nevertheless, such ligand-capped metal NCs suffer from low photocatalytic activity due to the lack of active sites. In addition, owing to their high surface energy, ultrasmall metal NCs tend to aggregate under light irradiation, resulting in mutable optical properties or diminished electron transfer capability [20,22–24]. These fatal demerits (lack of active sites, and thermodynamically unstable dispersion) largely impede their further development in photocatalysis. Accordingly, the main target for application of metal NCs in solar-driven CO₂ reduction is to graft active sites onto ligand-capping light absorbers while maintaining photostability. Although Au NCs that are grafted with metal cations as catalytic sites have obtained significantly achievements, these homogeneous Au NCs-based catalysts cannot be effectively purified from reaction systems and still encounter the low photostability due to easy agglomeration during prolonged reaction [25].

To address the above limitations, one promising approach is to confine Au NCs on a heterogeneous substrate with efficient catalytic sites. Ultrathin nanosheets, such as LDH, having accessible active sites and a large specific surface area, are great candidates as substrates for confining Au NCs [26–30]. However, the direct loading of ultrasmall Au NCs on a substrate commonly performs poorly in avoiding agglomeration [18,24]. Moreover, a bottleneck concomitantly emerges in regard to forming efficient electron transfer between Au NCs and catalytic sites, which holds the key to determining the efficiency for charge transfer and separation. Herein, we developed an effective strategy for bridging Au NCs with ultrathin LDH nanosheets via ligand engineering. The bridging ligands can function as surface anchors to confine and stabilize Au NCs on LDH, obviously inhibiting the agglomeration of Au NCs and thus enhancing the durability. Furthermore, transient absorption spectroscopy revealed that bridging ligands also can serve as electron mediators to facilitate electron transfer from Au NCs to catalytic sites, which remarkably boosts the efficiency for CO₂ reduction. Particularly, it is feasible to alter bridge ligands (e.g., 3-mercaptopropionic acid, 4-mercaptopropionic acid and 2-mercaptopropionic acid) and grafting substrates (e.g., CoAl-LDH and ZnAl-LDH) to modulate their catalytic activity and selectivity for solar-driven CO₂ reduction. This work provides a new strategy for stabilizing nanoclusters and enhancing the electron transfer between light-harvesting nanoclusters and catalytic sites through engineering bridging ligands.

2. Experimental section

2.1. Synthesis of Au-GSH NCs

Au-GSH NCs were synthesized according to our previously reported work [25]. First, 291 mg of HAuCl₄·4H₂O and 300 mg of L-glutathione were dissolved in 180 mL of deionized water with stirring at room temperature in a 250 mL conical flask. The mixture was stirred for about 1.5 h until the solution turned colorless. Then, the mixture in flask was heated by oil bath and kept at 70 °C under constant stirring for 24 h, followed by cooling to room temperature. The nanoclusters were purified by adding acetonitrile (3:1 vol ratio) to the solution containing as-prepared Au-GSH NCs. This solution was mixed thoroughly and centrifuged at 8000 rpm for 5 min. Finally, the supernatant was discarded, and the remaining sediments were redispersed in a small amount water and ultrasonicated, and then washed three times with the mixture of deionized water and acetonitrile (1:3 vol ratio). The purified Au-GSH NCs were redispersed in 10 mL of deionized water for further use. The specific concentration of Au NCs was confirmed by inductively-coupled plasma mass spectrometry.

2.2. Functionalization of Au-GSH NCs with L-cysteine (L-cys), 3-mercaptopropionic acid (3-MPA), 4-mercaptopropionic acid (4-MBA) and 2-mercaptopropionic acid (2-MBA)

10 mL of Au-GSH NCs aqueous dispersion (1 mg mL⁻¹) and 60 mL of

2-(N-morpholino) ethane sulfonic acid buffer (3.9 mg mL⁻¹) were added into a 250 mL round-bottom flask, followed by heating to 65 °C. Then, 36 mg of 1-(3(dimethylamino)propyl)-3-ethylcarbodiimide hydrochloride and 9.6 mg of N-hydroxysuccinimide were added into the flask as catalysts to drive the reaction for forming amide bond between –COOH of Au-GSH NCs and –NH₂ of L-cys. Subsequently, the solution was stirred for 15 min and 240 mg of L-cys was added into the mixture, followed by 6 h reaction at 65 °C under stirring. The prepared L-cys-modified Au-GSH (Au_{L-cys}) NCs were collected by centrifuging 5 min at 8000 rpm and washing three times with deionized water. Finally, 5 mL of deionized water was added into the purified Au_{L-cys} NCs, and 30 μL of NaOH (30 wt%) was added timely for better dispersion of Au_{L-cys} NCs in aqueous solution. The procedures for functionalizing Au-GSH NCs with 3-MPA, 4-MBA and 2-MBA are similar to that for functionalizing with L-cysteine.

2.3. Synthesis of NiAl-LDH, ZnAl-LDH and CoAl-LDH nanosheets

NiAl-LDH nanosheets were prepared according to previously reported method [31]. Typically, 100 mL of solution containing 37.5 mM Ni(NO₃)₂·6H₂O and 12.5 mM Al(NO₃)₃·9H₂O was added dropwise into 100 mL of formamide aqueous solution (23 vol%) at 80 °C under magnetic stirring. Simultaneously, 0.25 M NaOH aqueous solution was added dropwise into the above solution to keep the pH at ~10. After 10 min reaction, the NiAl-LDH nanosheets product was collected by centrifuging and washing with ethanol twice and water three times. Finally, the samples were freeze-dried for 48 h. ZnAl-LDH and CoAl-LDH were prepared following the same method.

2.4. Synthesis of Au-NA_{L-cys}, Au-NA_{3-MPA}, Au-NA_{2-MBA} and Au-NA_{4-MBA}

20 mg NiAl-LDH nanosheets were dispersed in 5 mL Au_{L-cys} solution (1 mg mL⁻¹), followed by stirring for 3 h. Then, the product was collected by centrifugation at 8000 rpm and subsequently washed with ultrapure water. Finally, the Au-NA_{L-cys} powder was obtained by freeze-drying for 48 h. Au-NA_{3-MPA}, Au-NA_{2-MBA} and Au-NA_{4-MBA} were prepared following the same procedures by dispersing 20 mg NiAl-LDH nanosheets in 5 mL Au_{3-MPA}, Au_{2-MBA} and Au_{4-MBA} solution (1 mg mL⁻¹), respectively.

2.5. Photocatalytic CO₂ reduction measurements

Photocatalytic CO₂ reduction measurements were carried out in a homemade quartz tube. First, Au-NA_{L-cys} (5 mg) was dispersed in mixed acetonitrile/water/triethanolamine solution (5 mL, volume ratio 3:1:1). Before performing photocatalytic CO₂ reduction, the tube was evacuated by a pump and refilled with pure CO₂ (Nanjing Ningte Gas Comp. 99.999%) three times in total. The performance of each photocatalyst was tested under stirring with a 300 W Xe lamp under full spectrum. The gaseous product was analyzed by gas chromatography (GC, 7890 A, Ar carrier, Agilent) equipped with a flame ionization detector (FID) and thermal conductivity detector (TCD). The isotopic experiment was carried out under a similar condition except using ¹³CO₂ (Linde Gas Comp. 99%) and the product was analyzed by gas chromatography–mass spectrometry (GC–MS, 7890A-5975 C, He carrier, Agilent). For the recycling test, the amounts for evolved CO and H₂ over Au-NA_{L-cys} photocatalyst were analyzed every 4 h and each cycle takes 12 h. After 12 h photocatalytic reaction, the samples were separated by centrifugation and washed with ultrapure water for three times, and then redispersed into the mixed acetonitrile/water/triethanolamine solution (5 mL, volume ratio 3:1:1) for another cycle.

2.6. Ultrafast transient absorption (TA) measurements

All the ultrafast TA measurements were carried out with a standard transmission pump–probe (UV/vis pump-broadband supercontinuum probe) instrument based on a 1-KHz Ti:sapphire regenerative amplifier

(Spitfire Ace, Spectra Physics, Inc.). The output pulsed laser from the amplifier with the center wavelength set at 800 nm and pulse width adjusted to be ~ 80 fs was split into several laser beams, one of which was used to generate wavelength-tunable light serving as the pump laser for TAS via a downstream TOPAS instrument. In this work, the TOPAS output was adjusted to be centered at 400 nm to photoexcite the samples. Another portion of the amplifier output beam was first fed into an optical delay line, then focused into the a CaF_2 crystal to generate the supercontinuum white light in the visible wavelength region. The 400-nm pump pulse was then chopped to 500 Hz and attenuated to 150 nJ/pulse. Finally, both the pump and probe pulses were focused and overlapped into a 2-mm sample cell. The TA signals were then collected by taking account for the intensity difference between the pump-on and pump-off absorption signals of the white light probe pulse. The delay time between the two pulses were continually scanned by the optical delay line during the data collection. The samples were constantly stirred during the TA measurements to avoid the sample sedimentation.

3. Results and discussion

3.1. Synthesis and structure characterizations

As a proof of concept, we chose glutathione-capped Au (Au-GSH) NCs and NiAl-LDH as the model materials, considering their intrinsic unique properties and facile preparation methods [31,32]. As shown in Fig. 1a, the water-soluble Au-GSH NCs with an average size of 1.51 nm were successfully fabricated, which endows a favorable visible light absorption (Fig. S1). Then, we intended to graft Au-GSH NCs onto NiAl-LDH via coordination interaction between the functional groups of peripheral ligands on Au-GSH and the catalytic metal sites on NiAl-LDH. Usually the capping ligands on Au-GSH NCs mainly provide the function groups of $-\text{NH}_2$ and $-\text{COOH}$ as anchoring sites, which have a lower affinity as compared to $-\text{SH}$ groups [25]. To firmly bind Au-GSH NCs onto the substrate, we functionalized Au-GSH NCs with thiol-containing ligands by forming amide bonds between glutathione and L-cys via a facile dehydration condensation (Fig. S2) [33]. As such, the uncoordinated thiols introduced by L-cys provide a platform for anchoring various substrates with metal catalytic sites. The structure of Au-GSH NCs is well retained after the functionalization, and the L-cys modified Au-GSH ($\text{Au}_{\text{L-cys}}$) NCs endows a significantly enhanced visible light absorption (Fig. S3). Then, the ultrathin NiAl-LDH nanosheet was fabricated to serve as an ideal substrate with abundant metal catalytic sites

for anchoring $\text{Au}_{\text{L-cys}}$ NCs. The weak diffraction peak along (001) in X-ray diffraction (XRD) pattern of NiAl-LDH indicates the lack of long-range order and less stack along Z direction (Fig. S4), confirming the ultrathin structure [31].

Subsequently, we integrated the functionalized $\text{Au}_{\text{L-cys}}$ NCs with NiAl-LDH support (Fig. 1b) through coordination, denoted as $\text{Au-Na}_{\text{L-cys}}$. Transmission electron microscopy (TEM) image shows that $\text{Au-Na}_{\text{L-cys}}$ maintains the nanosheet structure (Fig. 1c). As confirmed by high-resolution TEM (HRTEM), the well-isolated Au NCs are successfully assembled with NiAl-LDH, showing lattice spacings of 0.15 nm and 0.23 nm, respectively (Fig. 1d). After loading Au NCs onto NiAl-LDH, the obtained composite still exhibits less stack along the Z direction (Fig. S4). The characteristic peak for Au NCs can hardly be observed in XRD pattern due to their small loading amount and poor crystallinity [21]. However, high-angle annular dark-field scanning transmission electron microscopy (HAADF-STEM) and energy-dispersive X-ray spectroscopy (EDS) (Fig. 1e–h) verify the uniform dispersion of Au NCs on NiAl-LDH nanosheets. To examine the optical properties of $\text{Au-Na}_{\text{L-cys}}$ composite, UV–visible absorption spectra were investigated (Fig. S5). $\text{Au-Na}_{\text{L-cys}}$ exhibits excellent light absorption with the extended absorption band at 645–710 nm, which results from the spin–orbit coupling corresponding to the $^3\text{A}_2\text{g}(\text{F}) \rightarrow ^3\text{T}_{1\text{g}}(\text{F})$ transition of NiAl-LDH [34].

To further confirm the connection between light absorber and catalytic sites in $\text{Au-Na}_{\text{L-cys}}$ composite, X-ray photoelectron spectroscopy (XPS) was collected to analyze their bridging interaction. As depicted in Fig. 2a, the peaks of Au 4f in $\text{Au-Na}_{\text{L-cys}}$ shift about 0.8 eV toward lower binding energy compared to that of Au NCs, indicating that the electron density of Au atoms increases benefiting from the electron donation by $-\text{NH}_2$ in the L-cys. Moreover, the Ni 2p XPS peaks of $\text{Au-Na}_{\text{L-cys}}$ shift toward lower binding energy by about 0.7 eV in comparison with that of pristine NiAl-LDH (Fig. 2b), revealing that the electron density of Ni increases after the integration. In contrast, the S 2p XPS peaks of $\text{Au-Na}_{\text{L-cys}}$ shift about 0.6 eV toward higher binding energy compared to that of $\text{Au}_{\text{L-cys}}$ NCs (Fig. 2c), indicating the reduction in electron density of S in $\text{Au-Na}_{\text{L-cys}}$. Based on the above information, we suppose that the $-\text{SH}$ groups are coordinated with Ni sites for their available empty 3d orbital and the charge transfer should take place through the coordinated Ni–S interaction. Fourier transform infrared spectroscopy (FTIR) further confirms that the amide bond is formed as a bridge connection. As shown in Fig. 2d, the typical characteristic peaks at 1381 cm^{-1} (C–N stretching), 1530 cm^{-1} (N–H bending) and 1640 cm^{-1} (C=O

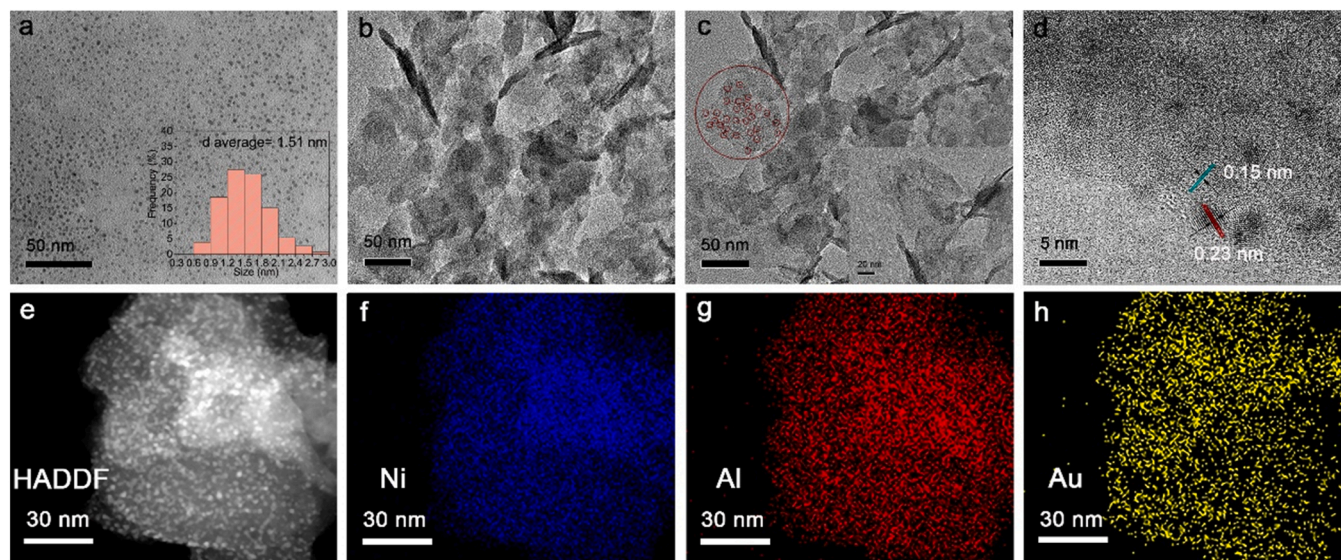


Fig. 1. TEM images of (a) Au NCs, (b) NiAl-LDH nanosheets and (c) $\text{Au-Na}_{\text{L-cys}}$ LDH nanosheets. (d) HRTEM image of $\text{Au-Na}_{\text{L-cys}}$. (e–h) HAADF-STEM image and EDS elemental mapping profiles of $\text{Au-Na}_{\text{L-cys}}$ with Ni (green), Al (red) and Au (yellow) distribution.

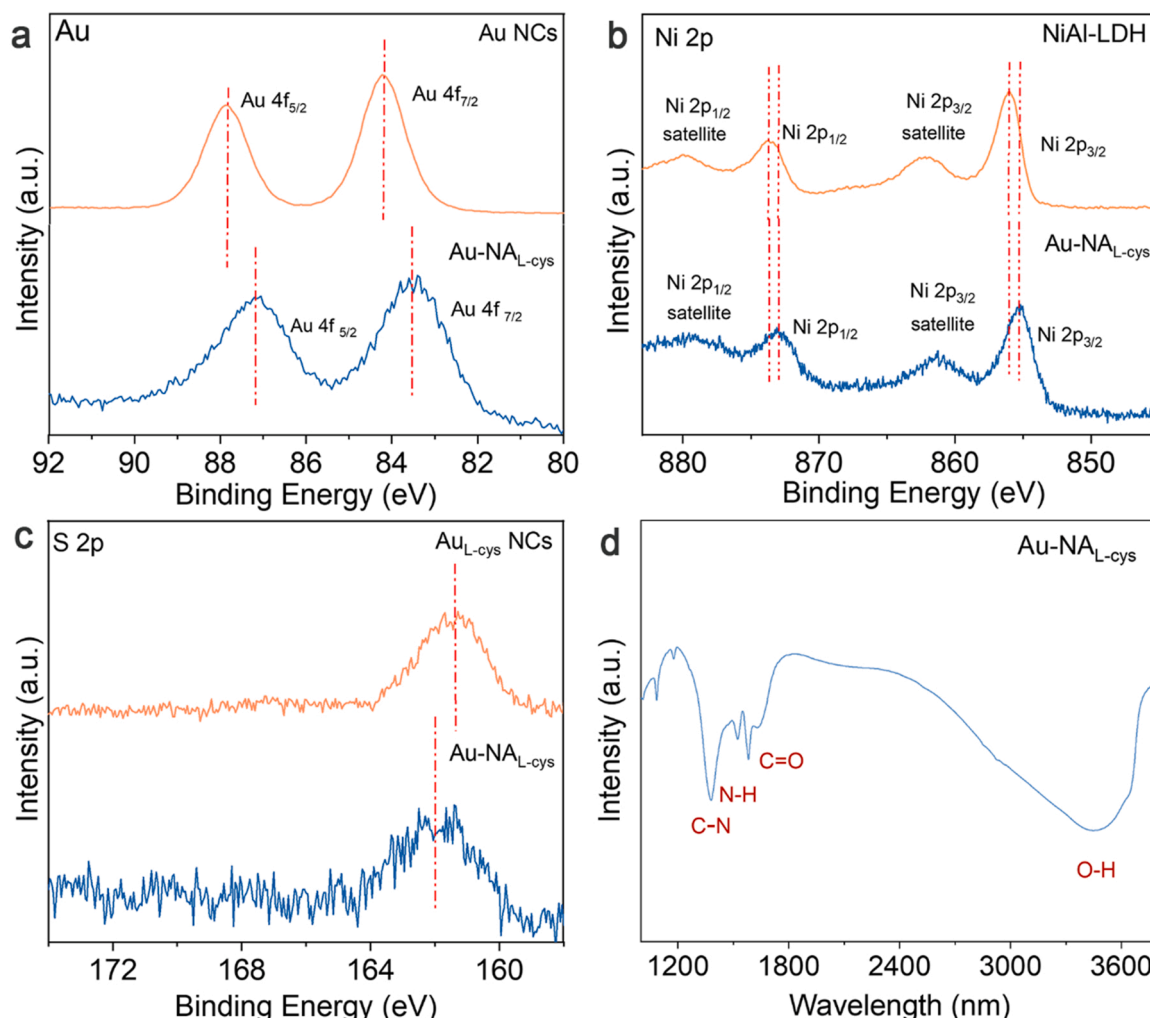


Fig. 2. (a) High-resolution Au 4f XPS spectra of Au NCs and Au-NA_{L-cys}. (b) High-resolution Ni 2p XPS spectra of NiAl-LDH and Au-NA_{L-cys}. (c) High-resolution S 2p XPS spectra of Au_{L-cys} NCs and Au-NA_{L-cys}. (d) FTIR spectra of Au-NA_{L-cys}.

stretching) in FTIR spectra of Au-NA_{L-cys} can be ascribed to the newly formed peptide bonds [25].

3.2. Photocatalytic performance

After having successfully fabricated the binary Au-NA_{L-cys} photocatalyst, we then evaluate its photocatalytic performance for CO₂ reduction. The photocatalytic experiments were performed under full-spectrum illumination in acetonitrile/water/triethanolamine (volume ratio 3:1:1) solution. As shown in Fig. 3a, the pristine Au NCs and NiAl-LDH are almost inactive for photocatalytic CO₂ conversion. After integrating Au NCs with NiAl-LDH via ligand L-cysteine, Au-NA_{L-cys} shows a remarkably enhanced activity for photocatalytic CO₂ reduction, with the CO and H₂ evolution rates of 3.64 μmol g⁻¹ h⁻¹ and 3.19 μmol g⁻¹ h⁻¹, respectively (Fig. 3a). To exclude the possibility that carbon source might be decomposed from the ligands, we conducted the isotope labeling experiment by feeding ¹³CO₂ gas (Fig. 3b). The signal at *m/z* = 29 in mass spectra is ascribed to ¹³CO, while the signals at *m/z* = 13 and *m/z* = 16 are attributed to related fragments of ¹³C and ¹⁶O. This result demonstrates that the produced CO indeed originates from the photocatalytic CO₂ conversion. Subsequently, the primary concern is the photostability of Au NCs, which has been a long-standing obstacle as stated in previous reports [18,35,36]. We performed long-time illumination experiments and cycling tests over Au-NA_{L-cys} photocatalyst to examine the photostability of Au NCs supported on NiAl-LDH. As shown

in Fig. 3c, after 3 cycles of 36 h reaction, Au-NA_{L-cys} can retain the original reaction rate and high dispersion of Au NCs on NiAl-LDH without agglomeration (average size ~1.52 nm, Fig. S6). The XPS and XRD characterizations indicate that the phase and elemental valence states of the Au-NA_{L-cys} catalyst have no significant change after 36 h photocatalytic reaction (Figs. S7 and S8), further validating its excellent stability during photocatalytic CO₂ conversion reaction. Furthermore, the stability of Au-NA_{L-cys} under various intensities of illumination (200–800 mW cm⁻²) was examined (Fig. S9). The activity for CO and H₂ evolution is enhanced with the increased light intensities and the Au NCs can still retain high dispersion with a mean size of 1.52 nm even under illumination with high light intensity (Fig. S10). In contrast, the pristine Au NCs in homogeneous solutions were aggregated after 10 h of full-spectrum illumination, and the average size of Au NCs increased significantly (Fig. S11). Particularly, the original clear solution turned to a suspension with sediment evolution after 10 h illumination under 800 mW cm⁻² (Fig. S12). The above results demonstrate that the stability of Au NCs is remarkably enhanced after being confined on NiAl-LDH nanosheets via bridging ligand.

Beyond confining the Au NCs on NiAl-LDH, the bridge ligand should have played an essential role in determining the electron transfer between Au NCs and catalytic sites. Thus a series of control experiments were conducted to further identify the role of bridging ligand in Au-NA_{L-cys} for photocatalytic CO₂ reduction. The physical mixture of Au NCs and NiAl-LDH exhibits distinctly lower CO evolution rate (2.77 μmol g⁻¹ h⁻¹)

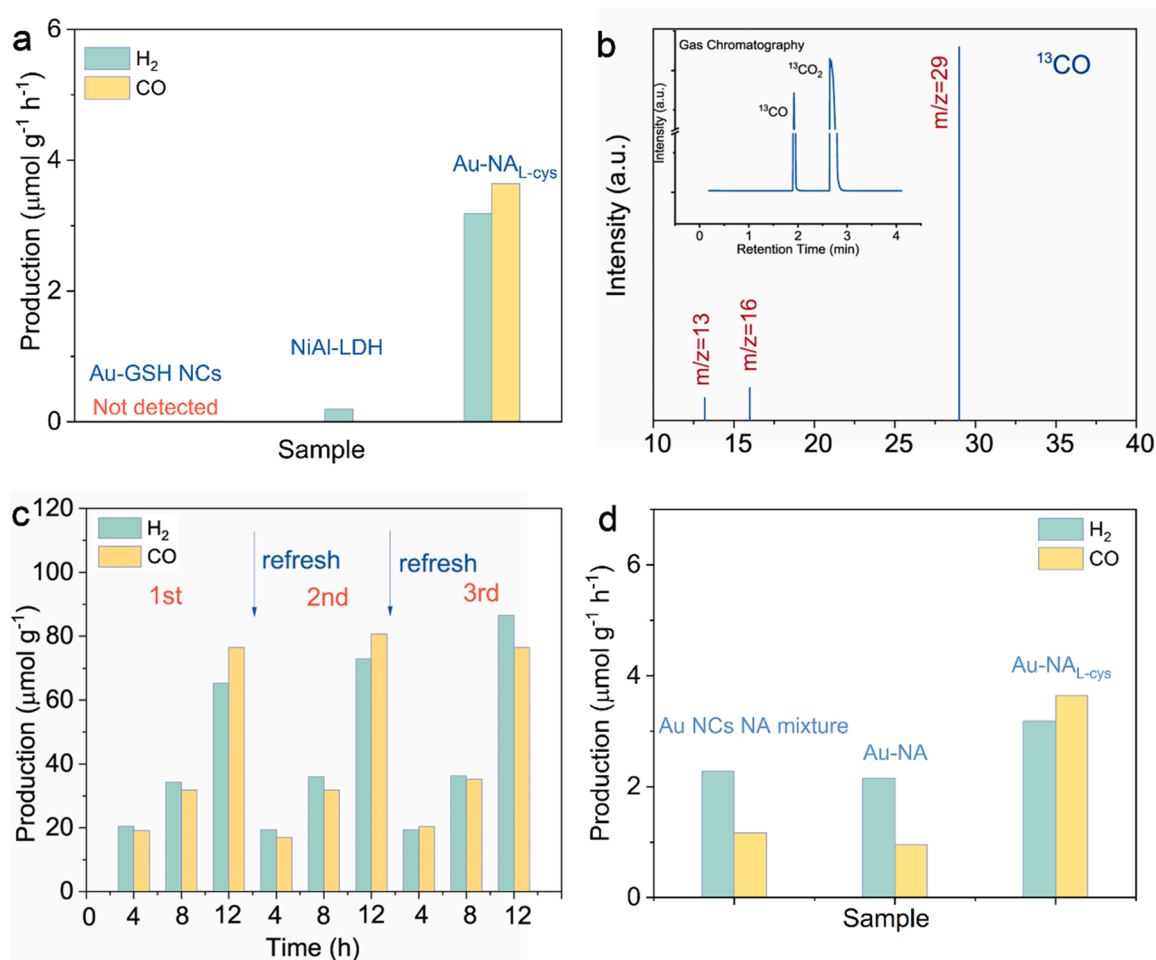


Fig. 3. (a) Production rates of CO and H₂ in photocatalytic CO₂ reduction by Au-GSH NCs, NiAl-LDH and Au-NA_{L-cys} catalyst under full-spectrum irradiation. (b) GC-MS data of ¹³CO produced from photocatalytic reduction of isotope-labeled ¹³CO₂ over Au-NA_{L-cys}. (c) The amounts for CO and H₂ evolution in cycling tests over Au-NA_{L-cys} photocatalyst. Each cycle takes 12 h. (d) Production rates of CO and H₂ evolution in photocatalytic CO₂ reduction over Au-NCs NA mixture, Au-NA and Au-NA_{L-cys} under full-spectrum irradiation of 4 h.

in contrast to Au-NA_{L-cys} (Fig. 3d), as the random collision in solution between light-harvesting Au NCs and catalytic NiAl-LDH impedes the effective electron transfer. Accordingly, we also assembled Au NCs onto NiAl-LDH without ligand connection (denoted as Au-NA) by the electrostatic interaction between negative Au-GSH NCs and positive NiAl-LDH [37,38]. TEM images of Au-NA show that Au NCs with an average size of 1.31 nm are integrated and dispersed uniformly on NiAl-LDH nanosheets (Fig. S13a and b). However, the photocatalytic performance of Au-NA is sharply reduced in contrast to Au-NA_{L-cys} regarding CO evolution (1.95 μmol g⁻¹ h⁻¹) and H₂ evolution (3.66 μmol g⁻¹ h⁻¹), due to the inferior ability of electron transfer between electrostatic adsorbed Au NCs and NiAl-LDH. Moreover, after 10 h full-spectrum illumination, Au NCs in Au-NA formed agglomeration with an average size of 1.89 nm and a few scattered nanoparticles with the size of ~5 nm emerged (Fig. S13c and d). This further confirms that the bridging ligands play an important role in firmly anchoring Au NCs onto NiAl-LDH nanosheets in uniform dispersion, thereby stabilizing the ultrasmall Au-GSH NCs by hampering their migration.

3.3. Mechanism investigation

To verify the role of bridging ligands in facilitating electron transfer, photocurrent response and transient fluorescence spectroscopy were employed to understand the behavior of charge separation and transfer. As revealed in Fig. 4a, after the introduction of bridging ligand, Au-NA_{L-}

cys exhibits an obviously enhanced photocurrent response with respect to those of Au-NA and NiAl-LDH. This increase in photocurrent responses is attributed to the favorable electron transfer from Au NCs to NiAl-LDH. Furthermore, Au-NA_{L-cys} shows an average decay lifetime of 12.48 ns as revealed in transient fluorescence spectrum (Fig. 4b, Table S1), while the average decay lifetimes for Au-NA and NiAl-LDH are shortened to 8.54 and 2.91 ns, respectively. Such a shortened decay lifetime over Au-NA further confirms the role of bridging ligands as an efficient electron transfer channel in facilitating charge separation and transfer during photocatalytic CO₂ reduction reaction [39,40].

Upon recognizing efficient charge transfer, in situ diffuse reflectance infrared Fourier transform spectroscopy (DRIFTS) was conducted to further explore the mechanism for CO₂ to CO conversion. As shown in Fig. 4c, due to the dissolution of CO₂ in water, the observed signals at 1290 and 1350 cm⁻¹ can be ascribed to the vibration signals of m-CO₃²⁻ group and the asymmetric O=C=O stretching vibration signals of b-CO₃²⁻, respectively [41,42]. After light irradiation, the emerged signal at 1640 cm⁻¹ can be ascribed to the stretching vibration of COOH*, which is the key intermediate for CO generation from CO₂ reduction [33,43,44]. Simultaneously, the signal at 2210 cm⁻¹ attributed to adsorbed CO appears after light irradiation and its intensity increases with illumination time. Based on above information, the overall catalytic reaction for the reduction of CO₂ to CO over Au-NA_{L-cys} photocatalyst can be summarized as the following steps (Fig. 4d):



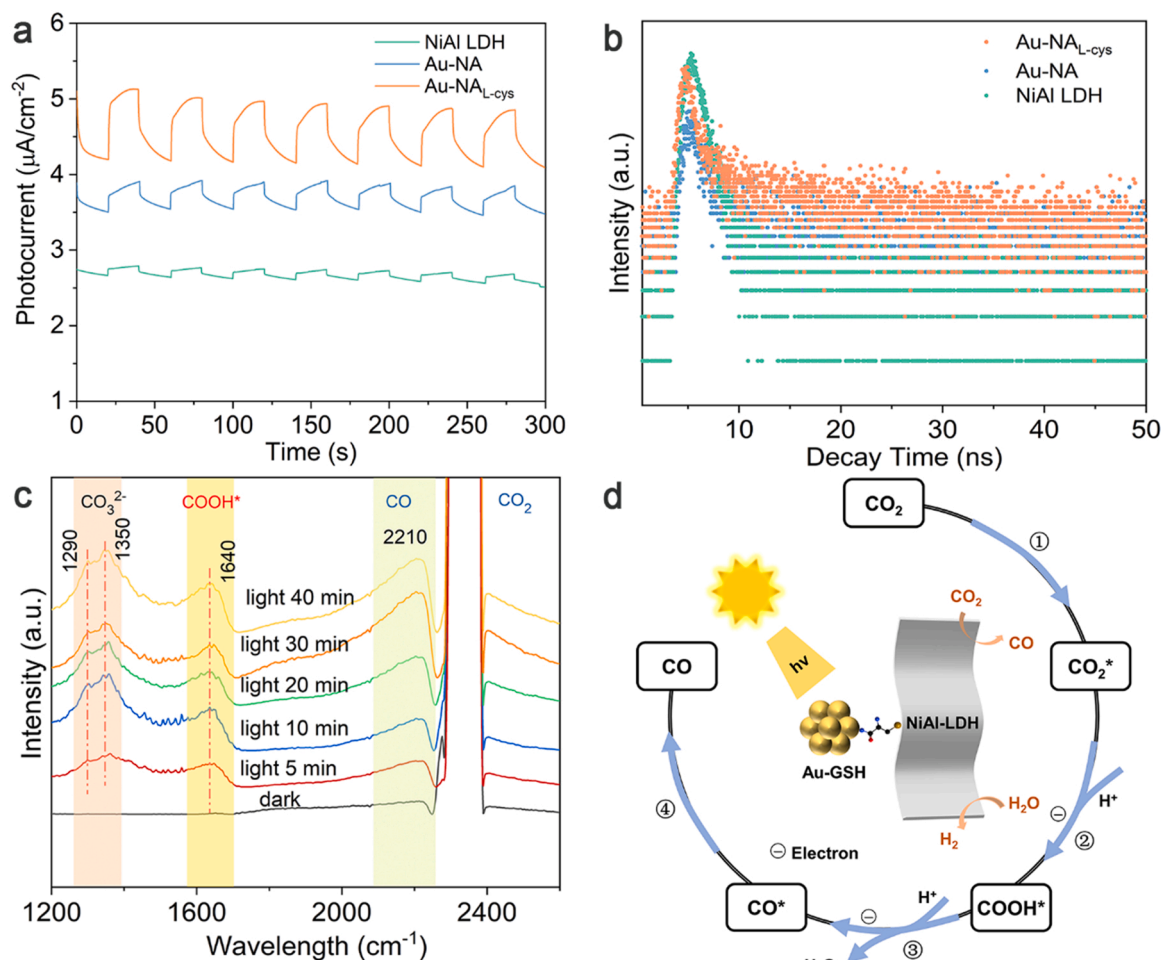


Fig. 4. (a) Photocurrent density over NiAl-LDH, Au-NA_{L-cys} and Au-NA under chopped light irradiation. (b) Transient fluorescence spectra of NiAl-LDH, Au-NA_{L-cys} and Au-NA. (c) In-situ DRIFTS spectra over Au-NA_{L-cys} for photocatalytic CO₂ reduction. (d) Schematic mechanistic pathway for CO₂ reduction reaction catalyzed by Au-NA_{L-cys}.



3.4. Engineering bridging ligands

Given the crucial role of bridging ligands in facilitating electron transfer, we further attempted to regulate the photocatalytic performance of Au NCs/NiAl-LDH hybrid system via engineering bridging ligands. As has been indicated by our characterization, the efficient electron transfer between light-harvesting Au NCs and catalytic NiAl-LDH in Au-NA_{L-cys} is enabled by Ni–S coordination via bridging L-cys ligand. The bridging ligands in our approach preferably contain one –COOH (or –NH₂) functional group and one –SH functional group, for simultaneously connecting with Au-GSH NCs and NiAl-LDH via amide bond and Ni–S coordination, respectively. In this regard, we compared L-cys with other three different bridging ligands that meet the above criterion, including 3-mercaptopropionic acid (3-MPA), 4-mercaptopbenzoic acid (4-MBA) and 2-mercaptopbenzoic acid (2-MBA), and their structures are shown in Fig. S14. Firstly, we compared the performance of Au NCs/NiAl-LDH composites with L-cys (with –NH₂ group) and 3-MPA (without –NH₂ group) as bridging ligands for photocatalytic CO₂

reduction. As shown in Fig. 5a, the Au-NA_{3-MPA} photocatalyst exhibited superior production rates for CO/H₂ evolution to Au-NA_{L-cys}. The molecular structure of 3-MPA is quite similar to that of L-cys except the absence of –NH₂ group in 3-MPA, leading to their different charge densities of –SH group. Owing to its high electronegativity than S atom, the N atom possesses a stronger negative induction effect, which makes the charge density of –SH group in L-cys lower than that in 3-MPA and leads to the weaker Ni–S interaction over Au-NA_{L-cys} [25]. As such, the absence of –NH₂ group in Au-NA_{3-MPA} can offer more efficient electron transfer, thereby enhancing photocatalytic performance.

As the bridging ligand can largely facilitate electron transfer by serving as an electron channel, we suppose that the conjugated ligands engendering delocalized π electrons along their backbone would perform even better for electron transfer [45,46]. Hence, we further modulated the bridging ligand in our photocatalytic system by two conjugated ligands — 4-MBA and 2-MBA, which are positional isomers with different relative positions of sulfhydryl. Interestingly, both Au-NA_{4-MBA} and Au-NA_{2-MBA} display significantly enhanced production rates for CO/H₂ evolution in photocatalytic CO₂ reduction in contrast to Au-NA_{L-cys} and Au-NA_{3-MPA} (Fig. 5a), suggesting that the superior charge separation and transfer efficiency of conjugated bridging ligands can improve photocatalytic activity. This argument is verified by examining the photocurrent response and transient fluorescence spectroscopy (Fig. S15 and Table S2), in which Au-NA_{4-MBA} exhibits higher photocurrent and longer average fluorescence lifetime than Au-NA_{L-cys}. We also observed the change of selectivity for CO/H₂ evolution over

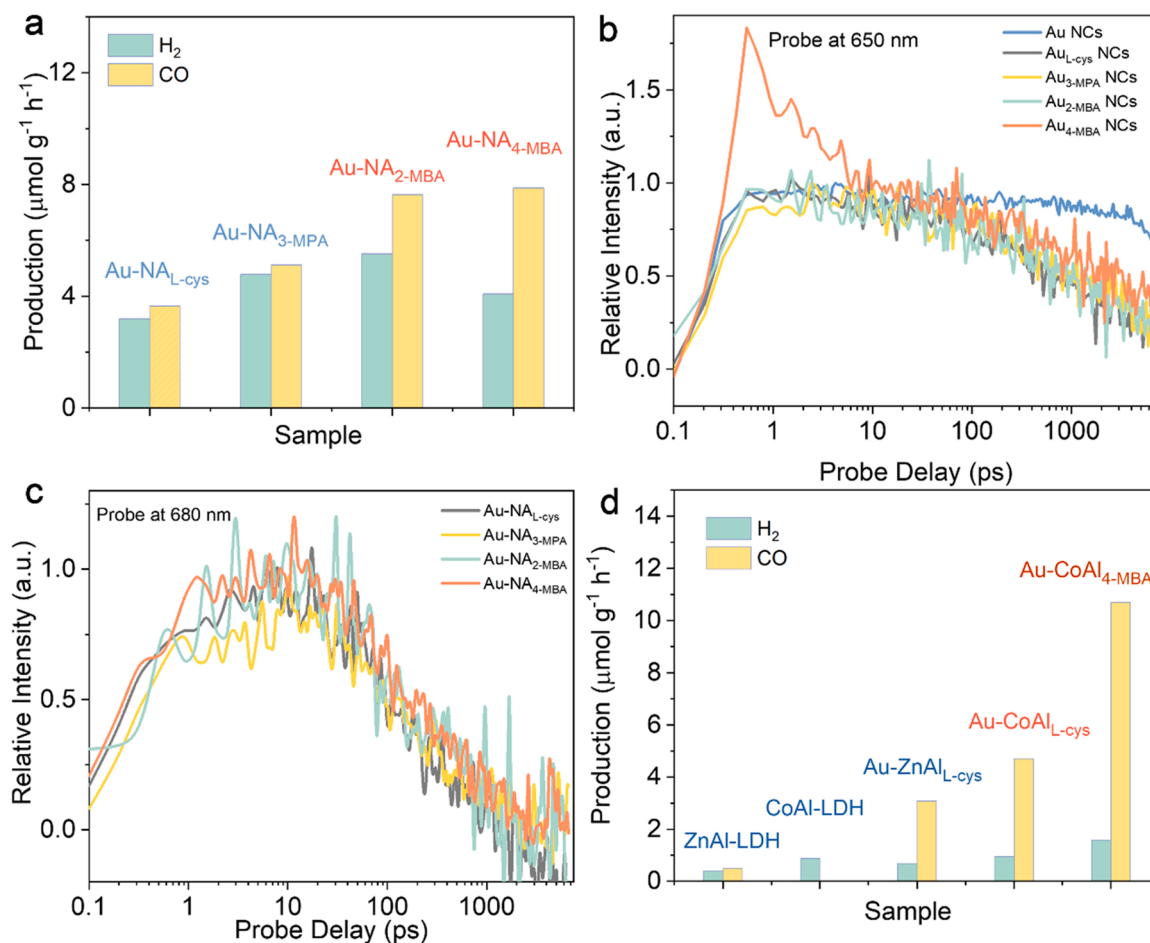


Fig. 5. (a) Production rates of CO and H₂ in photocatalytic CO₂ reduction by Au NCs/NiAl-LDH system with different bridging ligands. (b, c) The transient absorption-delay time profiles recorded at 650 nm for Au NCs (a) and 680 nm for Au NCs/NiAl-LDH (b) after pulsed 400 nm (150 nJ) photoexcitation. The kinetic traces are normalized. (d) Production rates of CO and H₂ in photocatalytic CO₂ reduction over ZnAl-LDH, CoAl-LDH, Au-ZnAl_{L-cys}, Au-CoAl_{L-cys} and Au-CoAl_{4-MBA} under full-spectrum irradiation of 4 h.

different bridging ligands (e.g., Au-NA_{L-cys} vs. Au-NA_{4-MBA}), which is probably attributed to the altered local electron density of catalytic sites via different bridging ligands.

The real-time electron transfer kinetics between Au NCs and NiAl-LDH were further explored by ultrafast transient absorption (TA) measurements. Broadband excited-state absorption (ESA) features are observed within the 450–700 nm range, which are consistent with the previous reports [47]. Fig. 5b and c include the typical decay kinetics of these transient ESA signals, while the fitting results of these kinetic traces are summarized in Fig. S16 and Table S3. Basically, the excited-state dynamics of Au NCs before the ligand functionalization is characterized with a rapid ESA signal rise within hundreds of femto-seconds and an extremely slow ESA decay with the time scale much longer than our 8 ns detection window, which can be attributed to the initial metal-to-metal (M-M) transition and the subsequent long-lived metal-to-ligand charge transfer (MLCT) state, respectively. The lifetime of MLCT state is significantly shortened to less than 1 ns after the functionalization of Au NCs (Fig. 5b and Table S3), most likely due to the alternation of electronic structures and charge recombination dynamics caused by the bridge ligands. It is noted that the 4-MBA capped Au NCs show an additional fast decay component (~3 ps). However, such a fast decay usually does not account for electron transfers, and thus is not the focus of the current work. Most importantly, the MLCT lifetime is further reduced by about three times when Au NCs are grafted onto the NiAl-LDH substrates (Figs. 5c, S16 and Table S3), which provides the direct evidence for the ultrafast electron transfer from Au NCs to LDH

substrates through bridge ligands. A detailed examination for the influence of the different bridge ligands on the electron transfer rate constants (k_{ET}) can also be achieved by comparing the corresponding MLCT lifetimes (Table S4) [48,49]. It is revealed that the Au-NA_{L-cys} possesses the lowest electron transfer rate among the four samples, which may explain the less efficient photocatalytic capability of Au-NA_{L-cys} compared with Au-NA_{3-MPA}, Au-NA_{4-MBA} and Au-NA_{2-MBA} as shown in Fig. 5a. The rate constants show a positive correlation with the yield of CO. This suggests that the electron transfer from excited Au NCs to NiAl-LDH and the formation of Au NCs (h^+)/NiAl-LDH (e^-) play key roles in the CO₂ photoreduction processes reported here.

To further validate the versatility of our approach for assembling homogeneous Au NC on heterogeneous catalytic LDH substrate via bridging ligands, we further utilized CoAl-LDH and ZnAl-LDH nano-sheets as substrates to construct Au NCs/LDH photocatalyst (denoted as Au-CoAl_{L-cys} and Au-ZnAl_{L-cys}). As indicated by HADDF-STEM image and EDS elemental mapping (Figs. S17 and S18), Au NCs can also be separately and uniformly dispersed on CoAl- and ZnAl-LDH supports. Encouragingly, Au-CoAl_{L-cys} and Au-ZnAl_{L-cys} photocatalyst endowed the photocatalytic CO₂ reduction with significantly enhanced selectivity for CO evolution in contrast to Au-NA_{L-cys} (Fig. 5d). Excitingly, when Au NCs were assembled on CoAl-LDH via 4-MBA bridging ligand (denoted as Au-CoAl_{4-MBA}), the production rate of CO was greatly enhanced with a remarkably improved selectivity (approximately 90%) as compared with Au-NA_{4-MBA}, well exceeding the performance of the state-of-the-art LDH- and metal nanoclusters-based photocatalysts for CO₂ reduction to

CO (Table S5). These results confirm that our approach for assembling homogeneous Au NC via bridging ligands is applicable to various LDH materials.

4. Conclusion

In summary, we have successfully confined homogeneous Au NCs on various heterogeneous LDH nanosheets to construct a binary Au NCs/LDH photocatalytic system via engineering bridging ligands. This strategy efficiently addresses the limitations of Au NCs in photocatalytic application regarding stability and activity. Moreover, the bridging ligands have been confirmed to play an essential role in determining the electron transfer between light-harvesting Au NCs and catalytic LDH. The conjugated bridging ligands serving as electron mediators between Au NCs and LDH endow the superior charge separation and transfer efficiency. It is also feasible to tune the local electron density of catalytic sites through modulating the bridging ligands, providing great opportunities for optimizing the performance over Au NCs/LDH photocatalyst. This work not only provides a versatile strategy for assembling homogeneous Au NCs on heterogeneous support with various catalytic metal sites, but also provide a fresh insight for regulating charge transfer and catalytic sites through engineering bridging ligands.

CRediT authorship contribution statement

Yanan Bo: Investigation, Writing - original draft. **Pengye Du:** Investigation. **Hao Li:** Investigation. **Rong Liu:** Investigation. **Chengming Wang:** Investigation. **Hengjie Liu:** Investigation. **Dong Liu:** Supervision, Writing - review & editing. **Tingting Kong:** Conceptualization, Supervision, Writing - review & editing. **Zhou Lu:** Methodology, Supervision, Writing - review & editing. **Chao Gao:** Supervision, Conceptualization, Writing - review & editing. **Yujie Xiong:** Conceptualization, Supervision, Writing - review & editing.

Declaration of Competing Interest

The authors declare that they have no known competing financial interests or personal relationships that could have appeared to influence the work reported in this paper.

Data availability

Data will be made available on request.

Acknowledgments

This work was financially supported by National Key R&D Program of China (2020YFA0406103), NSFC (91961106, 51902253, 22232003, 91963108, 22175165, 22073001, 22279128), Strategic Priority Research Program of the CAS (XDPB14), Open Funding Project of National Key Laboratory of Human Factors Engineering (No. SYFD062010K), Youth Innovation Promotion Association CAS (2021451), USTC Research Funds of the Double First-Class Initiative (YD2060002025), Fundamental Research Funds for the Central Universities (WK2340000104, WK2400000004), University Annual Scientific Research Plan of Anhui Province (2022AH010013), University Synergy Innovation Program of Anhui Province (GXXT-2021-049) and Gusu Innovation and Entrepreneurship Leading Talents Program (ZXL2022386). The authors thank the support from USTC Center for Micro- and Nanoscale Research and Fabrication.

Appendix A. Supplementary material

Supplementary data associated with this article can be found in the online version at [doi:10.1016/j.apcatb.2023.122667](https://doi.org/10.1016/j.apcatb.2023.122667).

References

- [1] W. Gao, S. Liang, R. Wang, Q. Jiang, Y. Zhang, Q. Zheng, B. Xie, C.Y. Toe, X. Zhu, J. Wang, L. Huang, Y. Gao, Z. Wang, C. Jo, Q. Wang, L. Wang, Y. Liu, B. Louis, J. Scott, A.-C. Roger, R. Amal, H. He, S.-E. Park, Industrial carbon dioxide capture and utilization: state of the art and future challenges, *Chem. Soc. Rev.* 49 (2020) 8584–8686, <https://doi.org/10.1039/D0CS00025F>.
- [2] S. Zhang, Q. Fan, R. Xia, T.J. Meyer, CO₂ reduction: from homogeneous to heterogeneous electrocatalysis, *Acc. Chem. Res.* 53 (2020) 255–264, <https://doi.org/10.1021/acs.accounts.9b00496>.
- [3] A. Wagner, C.D. Sahm, E. Reisner, Towards molecular understanding of local chemical environment effects in electro- and photocatalytic CO₂ reduction, *Nat. Catal.* 3 (2020) 775–786, <https://doi.org/10.1038/s41929-020-00512-x>.
- [4] C. Gao, J. Wang, H. Xu, Y. Xiong, Coordination chemistry in the design of heterogeneous photocatalysts, *Chem. Soc. Rev.* 46 (2017) 2799–2823, <https://doi.org/10.1039/C6CS00727A>.
- [5] C. Gao, Y. Xiong, Solar-driven artificial carbon cycle, *Chin. J. Chem.* 40 (2022) 153–159, <https://doi.org/10.1002/cjoc.202100549>.
- [6] C. Gao, S. Chen, Y. Wang, J. Wang, X. Zheng, J. Zhu, L. Song, W. Zhang, Y. Xiong, Heterogeneous single-atom catalyst for visible-light-driven high-turnover CO₂ reduction: the role of electron transfer, *Adv. Mater.* 30 (2018), e1704624, <https://doi.org/10.1002/adma.201704624>.
- [7] L. Tan, S.-M. Xu, Z. Wang, Y. Xu, X. Wang, X. Hao, S. Bai, C. Ning, Y. Wang, W. Zhang, Y.K. Jo, S.-J. Hwang, X. Cao, X. Zheng, H. Yan, Y. Zhao, H. Duan, Y.-F. Song, Highly selective photoreduction of CO₂ with suppressing H₂ evolution over monolayer layered double hydroxide under irradiation above 600 nm, *Angew. Chem. Int. Ed.* 58 (2019) 11860–11867, <https://doi.org/10.1002/anie.201904246>.
- [8] J. Nowotny, M.A. Alim, T. Bak, M.A. Idris, M. Ionescu, K. Prince, M.Z. Sahdan, K. Sopian, M.A. Mat Teridi, W. Sigmund, Defect chemistry and defect engineering of TiO₂-based semiconductors for solar energy conversion, *Chem. Soc. Rev.* 44 (2015) 8424–8442, <https://doi.org/10.1039/C4CS00469H>.
- [9] L. Ran, J. Hou, S. Cao, Z. Li, Y. Zhang, Y. Wu, B. Zhang, P. Zhai, L. Sun, Defect engineering of photocatalysts for solar energy conversion, *Sol. RRL* 4 (2020) 1900487, <https://doi.org/10.1002/solr.201900487>.
- [10] N. Zhang, C. Gao, Y. Xiong, Defect engineering: a versatile tool for tuning the activation of key molecules in photocatalytic reactions, *J. Energy Chem.* 37 (2019) 43–57, <https://doi.org/10.1016/j.jechem.2018.09.010>.
- [11] S. Bai, N. Zhang, C. Gao, Y. Xiong, Defect engineering in photocatalytic materials, *Nano Energy* 53 (2018) 296–336, <https://doi.org/10.1016/j.nanoen.2018.08.058>.
- [12] D. Maarisetty, S.S. Baral, Defect engineering in photocatalysis: formation, chemistry, optoelectronics, and interface studies, *J. Mater. Chem. A* 8 (2020) 18560–18604, <https://doi.org/10.1039/D0TA04297H>.
- [13] W. Zhou, H. Fu, Defect-mediated electron-hole separation in semiconductor photocatalysis, *Inorg. Chem. Front.* 5 (2018) 1240–1254, <https://doi.org/10.1039/C8QI00122G>.
- [14] R. Jin, C. Zeng, M. Zhou, Y. Chen, Atomically precise colloidal metal nanoclusters and nanoparticles: fundamentals and opportunities, *Chem. Rev.* 116 (2016) 10346–10413, <https://doi.org/10.1021/acs.chemrev.5b00703>.
- [15] R. Jin, Atomically precise metal nanoclusters: stable sizes and optical properties, *Nanoscale* 7 (2015) 1549–1565, <https://doi.org/10.1039/C4NR05794E>.
- [16] R. Jin, Y. Pei, T. Tsukuda, Controlling nanoparticles with atomic precision, 1–1, *Acc. Chem. Res.* 52 (2019), <https://doi.org/10.1021/acs.accounts.8b00631>.
- [17] M. Zhu, C.M. Aikens, F.J. Hollander, G.C. Schatz, R. Jin, Correlating the crystal structure of a thiol-protected Au₂₅ cluster and optical properties, *J. Am. Chem. Soc.* 130 (2008) 5883–5885, <https://doi.org/10.1021/ja801173r>.
- [18] Y.-S. Chen, P.V. Kamat, Glutathione-capped gold nanoclusters as photosensitizers. Visible light-induced hydrogen generation in neutral water, *J. Am. Chem. Soc.* 136 (2014) 6075–6082, <https://doi.org/10.1021/ja5017365>.
- [19] Y.-S. Chen, H. Choi, P.V. Kamat, Metal-cluster-sensitized solar cells. A new class of thiolated gold sensitizers delivering efficiency greater than 2%, *J. Am. Chem. Soc.* 135 (2013) 8822–8825, <https://doi.org/10.1021/ja403807f>.
- [20] X.-C. Dai, M.-H. Huang, Y.-B. Li, T. Li, S. Hou, Z.-Q. Wei, F.-X. Xiao, Probing the advantageous photosensitization effect of metal nanoclusters over plasmonic metal nanocrystals in photoelectrochemical water splitting, *J. Phys. Chem. C* 124 (2020) 4989–4998, <https://doi.org/10.1021/acs.jpcc.9b10132>.
- [21] F.-X. Xiao, Z. Zeng, B. Liu, Bridging the gap: electron relay and plasmonic sensitization of metal nanocrystals for metal clusters, *J. Am. Chem. Soc.* 137 (2015) 10735–10744, <https://doi.org/10.1021/jacs.5b06323>.
- [22] R. Jin, Y. Cao, C.A. Mirkin, K.L. Kelly, G.C. Schatz, J.G. Zheng, Photoinduced conversion of silver nanospheres to nanoprisms, *Science* 294 (2001) 1901–1903, <https://doi.org/10.1126/science.106654>.
- [23] S. Besner, A.V. Kabashin, F.M. Winnik, M. Meunier, Synthesis of size-tunable polymer-protected gold nanoparticles by femtosecond laser-based ablation and seed growth, *J. Phys. Chem. C* 113 (2009) 9526–9531, <https://doi.org/10.1021/jp809275v>.
- [24] P. Ramasamy, S. Guha, E.S. Shibu, T.S. Sreepasad, S. Bag, A. Banerjee, T. Pradeep, Size tuning of Au nanoparticles formed by electron beam irradiation of Au₂₅ quantum clusters anchored within and outside of dipeptide nanotubes, *J. Mater. Chem.* 19 (2009) 8456–8462, <https://doi.org/10.1039/B913405K>.
- [25] X. Cui, J. Wang, B. Liu, S. Ling, R. Long, Y. Xiong, Turning Au nanoclusters catalytically active for visible-light-driven CO₂ reduction through bridging ligands, *J. Am. Chem. Soc.* 140 (2018) 16514–16520, <https://doi.org/10.1021/jacs.8b06723>.
- [26] Y. Zhao, G.I.N. Waterhouse, G. Chen, X. Xiong, L.Z. Wu, C.H. Tung, T. Zhang, Two-dimensional-related catalytic materials for solar-driven conversion of COx into

- valuable chemical feedstocks, *Chem. Soc. Rev.* 48 (2019) 1972–2010, <https://doi.org/10.1039/C8CS00607E>.
- [27] Y. Zhao, X. Jia, G.I.N. Waterhouse, L.-Z. Wu, C.-H. Tung, D. O'Hare, T. Zhang, Layered double hydroxide nanostructured photocatalysts for renewable energy production, *Adv. Energy Mater.* 6 (2016), <https://doi.org/10.1002/aenm.201501974>.
- [28] Z. Qin, J. Wu, B. Li, T. Su, H. Ji, Ultrathin layered catalyst for photocatalytic reduction of CO₂, *Acta Phys. Chim. Sin.* 37 (2021) 2005027, <https://doi.org/10.3866/PKU.WHXB202005027>.
- [29] X. Cai, X. Sui, J. Xu, A. Tang, X. Liu, M. Chen, Y. Zhu, Tuning selectivity in catalytic conversion of CO₂ by one-atom-switching of Au₉ and Au₈Pd₁ catalysts, *CCS Chem.* 3 (2021) 408–420, <https://doi.org/10.31635/ccschem.021.202000730>.
- [30] Y.L. Huang, W. Chen, A.T.S. Wee, Two-dimensional magnetic transition metal chalcogenides, *SmartMat* 2 (2021) 139–153, <https://doi.org/10.1002/smm2.1031>.
- [31] J. Yu, B.R. Martin, A. Clearfield, Z. Luo, L. Sun, One-step direct synthesis of layered double hydroxide single-layer nanosheets, *Nanoscale* 7 (2015) 9448–9451, <https://doi.org/10.1039/c5nr01077b>.
- [32] Z. Luo, X. Yuan, Y. Yu, Q. Zhang, D.T. Leong, J.Y. Lee, J. Xie, From aggregation-induced emission of Au(I)–thiolate complexes to ultrabright Au(0)@Au(I)–thiolate core–shell nanoclusters, *J. Am. Chem. Soc.* 134 (2012) 16662–16670, <https://doi.org/10.1021/ja306199p>.
- [33] J. Wang, T. Xia, L. Wang, X. Zheng, Z. Qi, C. Gao, J. Zhu, Z. Li, H. Xu, Y. Xiong, Enabling visible-light-Driven selective CO₂ reduction by doping quantum dots: trapping electrons and suppressing H₂ evolution, *Angew. Chem. Int. Ed.* 57 (2018) 16447–16451, <https://doi.org/10.1002/anie.201810550>.
- [34] H. Wang, X. Xiang, F. Li, Facile synthesis and novel electrocatalytic performance of nanostructured Ni–Al layered double hydroxide/carbon nanotube composites, *J. Mater. Chem.* 20 (2010) 3944–3952, <https://doi.org/10.1039/B924911G>.
- [35] B. Weng, K.-Q. Lu, Z. Tang, H.M. Chen, Y.-J. Xu, Stabilizing ultrasmall Au clusters for enhanced photoredox catalysis, *Nat. Commun.* 9 (2018) 1543, <https://doi.org/10.1038/s41467-018-04020-2>.
- [36] F.-X. Xiao, Z. Zeng, S.-H. Hsu, S.-F. Hung, H.M. Chen, B. Liu, Light-induced in situ transformation of metal clusters to metal nanocrystals for photocatalysis, *ACS Appl. Mater. Interfaces* 7 (2015) 28105–28109, <https://doi.org/10.1021/acsami.5b09091>.
- [37] Z.-Q. Wei, S. Hou, X. Lin, S. Xu, X.-C. Dai, Y.-H. Li, J.-Y. Li, F.-X. Xiao, Y.-J. Xu, Unexpected boosted solar water oxidation by nonconjugated polymer-mediated tandem charge transfer, *J. Am. Chem. Soc.* 142 (2020) 21899–21912, <https://doi.org/10.1021/jacs.0c11057>.
- [38] R. Ma, Z. Liu, L. Li, N. Iyi, T. Sasaki, Exfoliating layered double hydroxides in formamide: a method to obtain positively charged nanosheets, *J. Mater. Chem.* 16 (2006), <https://doi.org/10.1039/b605422f>.
- [39] W. Shao, S. Wang, J. Zhu, X. Li, X. Jiao, Y. Pan, Y. Sun, Y. Xie, In-plane heterostructured Ag₂S–In₂S₃ atomic layers enabling boosted CO₂ photoreduction into CH₄, *Nano Res.* 14 (2021) 4520–4527, <https://doi.org/10.1007/s12274-021-3365-4>.
- [40] P. Xia, M. Antonietti, B. Zhu, T. Heil, J. Yu, S. Cao, Designing defective crystalline carbon nitride to enable selective CO₂ photoreduction in the gas phase, *Adv. Funct. Mater.* 29 (2019) 1900093, <https://doi.org/10.1002/adfm.201900093>.
- [41] L. Liu, Y. Jiang, H. Zhao, J. Chen, J. Cheng, K. Yang, Y. Li, Engineering coexposed {001} and {101} facets in oxygen-deficient TiO₂ nanocrystals for enhanced CO₂ photoreduction under visible light, *ACS Catal.* 6 (2016) 1097–1108, <https://doi.org/10.1021/acscatal.5b02098>.
- [42] X. Li, Y. Wei, C. Ma, H. Jiang, M. Gao, S. Zhang, W. Liu, P. Huo, H. Wang, L. Wang, Multichannel electron transmission and fluorescence resonance energy transfer in In₂S₃/Au/rGO composite for CO₂ photoreduction, *ACS Appl. Mater. Interfaces* 13 (2021) 11755–11764, <https://doi.org/10.1021/acsami.0c18809>.
- [43] X. Jiao, X. Li, X. Jin, Y. Sun, J. Xu, L. Liang, H. Ju, J. Zhu, Y. Pan, W. Yan, Y. Lin, Y. Xie, Partially oxidized SnS₂ atomic layers achieving efficient visible-light-driven CO₂ reduction, *J. Am. Chem. Soc.* 139 (2017) 18044–18051, <https://doi.org/10.1021/jacs.7b10287>.
- [44] Y. Li, M. Wen, Y. Wang, G. Tian, C. Wang, J. Zhao, Plasmonic hot electrons from oxygen vacancies for infrared light-driven catalytic CO₂ reduction on Bi₂O_{3-x}, *Angew. Chem. Int. Ed.* 60 (2021) 910–916, <https://doi.org/10.1002/anie.202010156>.
- [45] C. Dai, B. Liu, Conjugated polymers for visible-light-driven photocatalysis, *Energy Environ. Sci.* 13 (2020) 24–52, <https://doi.org/10.1039/C9EE01935A>.
- [46] Y. Liang, J.E. Thorne, M.E. Kern, B.A. Parkinson, Sensitization of ZnO single crystal electrodes with CdSe quantum dots, *Langmuir* 30 (2014) 12551–12558, <https://doi.org/10.1021/la5023888>.
- [47] K.G. Stamplecoskie, P.V. Kamat, Size-dependent excited state behavior of glutathione-capped gold clusters and their light-harvesting capacity, *J. Am. Chem. Soc.* 136 (2014) 11093–11099, <https://doi.org/10.1021/ja505361n>.
- [48] X. Lu, A. Tong, D. Luo, F. Jiang, J. Wei, Y. Huang, Z. Jiang, Z. Lu, Y. Ni, Confining single Pt atoms from Pt clusters on multi-armed CdS for enhanced photocatalytic hydrogen evolution, *J. Mater. Chem. A* 10 (2022) 4594–4600, <https://doi.org/10.1039/D2TA00198E>.
- [49] H. Zhu, N. Song, T. Lian, Charging of quantum dots by sulfide redox electrolytes reduces electron injection efficiency in quantum dot sensitized solar cells, *J. Am. Chem. Soc.* 135 (2013) 11461–11464, <https://doi.org/10.1021/ja405026x>.